

A Sub-pixel Accurate Quantification of Joint Space Narrowing Progression in Rheumatoid Arthritis

Yafei Ou^{ib}, Prasoon Ambalathankandy^{ib}, Ryunosuke Furuya, Seiya Kawada, Tianyu Zeng, Yujie An, Tamotsu Kamishima^{ib}, Kenichi Tamura, and Masayuki Ikebe^{ib}

Abstract—Rheumatoid arthritis (RA) is a chronic autoimmune disease that primarily affects peripheral synovial joints, like fingers, wrist and feet. Radiology plays a critical role in the diagnosis and monitoring of RA. Limited by the current spatial resolution of radiographic imaging, joint space narrowing (JSN) progression of RA with the same reason above can be less than one pixel per year with universal spatial resolution. Insensitive monitoring of JSN can hinder the radiologist/rheumatologist from making a proper and timely clinical judgment. In this paper, we propose a novel and sensitive method that we call partial image phase-only correlation which aims to automatically quantify JSN progression in the early stages of RA. The majority of the current literature utilizes the mean error, root-mean-square deviation and standard deviation to report the accuracy at pixel level. Our work measures JSN progression between a baseline and its follow-up finger joint images by using the phase spectrum in the frequency domain. Using this study, the mean error can be reduced to 0.0130mm when applied to phantom radiographs with ground truth, and 0.0519mm standard deviation for clinical radiography. With its sub-pixel accuracy far beyond manual measurement, we are optimistic that our work is promising for automatically quantifying JSN progression.

Index Terms—Rheumatoid Arthritis, Frequency Domain Analysis, Joint Space Narrowing, Phantom Imaging, Radiology, Computer-aided Diagnosis.

I. INTRODUCTION

Rheumatoid arthritis (RA) is a progressive, chronic autoimmune disease characterized by synovitis that can ultimately cause deformities and ankylosis in peripheral synovial joints and impair the movement and flexibility of digits, and as

Yafei Ou, Prasoon Ambalathankandy, Ryunosuke Furuya and Seiya Kawada are with the Research Center For Integrated Quantum Electronics, Hokkaido University, Sapporo 060-0813, Japan, and also with the Graduate School of Information Science and Technology, Hokkaido University, Sapporo 060-0814, Japan.

Tianyu Zeng and Yujie An are with the Graduate School of Health Sciences, Hokkaido University, Sapporo 060-0812, Japan.

Tamotsu Kamishima is with Faculty of Health Sciences, Hokkaido University, Sapporo 060-0812, Japan.

Kenichi Tamura is with Department of Mechanical Engineering, College of Engineering, Nihon University, Koriyama 963-8642, Japan.

Masayuki Ikebe is with the Research Center For Integrated Quantum Electronics, Hokkaido University, Sapporo 060-0813, Japan (e-mail: ikebe@ist.hokudai.ac.jp).

This work has been published in IEEE Journal of Biomedical and Health Informatics. DOI: [10.1109/JBHI.2022.3217685](https://doi.org/10.1109/JBHI.2022.3217685).

well as the patient's whole hand. The major radiographic changes on hand, wrist and feet joints are cartilage damage and bone destruction (like bone erosion and joint space narrowing (JSN)). Those damage and destruction typically lead to painful joints, progressive joint destruction, deformity, followed by functional limitation and severe disability [1], [2]. There are substantial evidence that RA can be managed in a low level of disease activity and clinical remission with disease-modifying antirheumatic drugs [3], [4]. Early diagnosis by precise quantification of subtle radiographic changes is essential for successful treatment, as it can improve outcomes and effectively manage the progression of RA [3], [4].

Radiology plays a crucial role in diagnosis and monitoring of RA. Clinical radiologist/rheumatologist can assess the radiographic progression of RA by using the Sharp/van der Heijde scoring method (SvdH). This method relies on scoring of the radiographies by subjectively assessing JSN and bone erosion of 38 hand or foot joints [5]. JSN progression is one of the most important indicators in RA treatment, as it can directly impact medication. Limited by the current spatial resolution of radiographic imaging, JSN progression over a period of one year can be less than one pixel, as show in Fig. 1. This means that the pixel-level accuracy algorithm requires more time to wait for the change of joint space. Nevertheless, this can lead to insensitive monitoring of JSN progression, and this may hinder the radiologist/rheumatologist from making a proper diagnosis in the "window of opportunity" [6]–[8].

In recent years, researchers have invested great efforts to study automatic quantification of joint space for RA diagnosis [9]–[24]. However, constrained by limited accuracy of related works, as shown in section IV-B, sensitively monitoring cartilage damage and bone destruction progression in the early stages of RA is a recognized challenge [9], [21]. The major benefit of this study compared to most extant ones is an attempt to improve sensitivity and accuracy of the JSN quantification algorithm to sub-pixel level so that rheumatologist can monitor the JSN progression in RA early stages on an annual basis.

The JSN progression quantification pipeline in radiographs is performed in two steps; joint position detection and joint space quantification.

1) *Related works about finger joint position detection*: The earliest studies about finger joint location detection were based

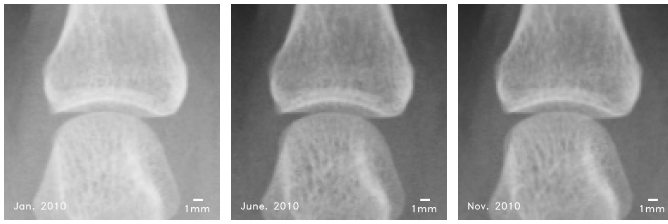


Fig. 1. JSN progression of a MCP joint for little finger over a period of 10 months. From left to right the images are: baseline, five-month, and ten-month images (spatial resolution: $0.175\text{mm}/\text{pixel}$). Usually, JSN progression is less than one pixel per year, therefore, it is difficult for radiologist/rheumatologist to see. Then, operating with an algorithm with pixel level accuracy to quantify JSN over a period of one year can be ineffective. JSN measured for five and ten months X-rays relative to baseline using our method are -0.111pixel and 0.213pixel respectively.

on using pixel information. Those algorithms extracted the finger midlines based on ridge detection, thus, finger joint location can be detected according to the gradient or intensity information of finger midline [18]–[21], [25]. However, these method may break finger midline at the metacarpophalangeal (MCP) joint because of decrease in bone density. And may mismatch joint position for the following reasons: (i) bone overlap caused by finger bending in the vertical plane. (ii) marginal density decrease caused by ankylosis or complete luxation [21].

In recent years, machine learning (ML) based methods have become a very important tool to solve complex medical image processing tasks [26]. It is widely used in image segmentation [27], computer aided diagnosis [28], image registration [29] and others [30]. For finger joint detection, there are some ML-based studies utilizing key point detection for convolutional neural network (CNN) [10], [11], support vector machine (SVM) [14], [15] and Haar-like adaptive boosting (AdaBoost) [23], [31]. Although these ML-based methods improve the detection accuracy, there are still several pixels deviation in the deduced joint position.

2) Literature survey of joint space quantification in RA: In the literature, detecting the upper and lower bone margins to measure the joint space width (JSW) is the most common program. They can be broadly grouped in to two groups; supervised ML-based [9]–[15] and image features based [16]–[21], such as intensity, gradient, derivative or differential. As a representative for early RA diagnosis, Huo proposed a fully automatic JSW quantification method [21]. Their work can be performed as follow: (i) Detect bone margin by using intensity and gradient information. (ii) Fit polynomial functions to bone margin curves. (iii) Quantify JSW according to the distance between polynomial function. As an exception, Kato et al. proposed a JSN quantification method without margin detection [22]. This method can monitor JSN by comparing the difference of pixel intensity between the baseline and its follow-up joint windows, which is more sensitive to JSN.

For analyzing joints of RA patients, some supervised ML-based studies have been proposed like Peloschek et al [9], [10]. They report a JSW quantification and erosion detection method based on key point detection by using active shape models (ASMs). Additionally, some studies have explored

CNN [11]–[13], and SVM [14], [15] to score radiographic joint destruction rather than trying to quantify the joint space. These studies grouped finger joints into five levels according to the SvdH scoring method [5]. Compared to other joint space quantification studies, scoring standard with only five or less levels limits the sensitivity and timeliness of the tool. Therefore, if it is not feasible to increase the number of scoring levels, that would make it difficult for radiologist/rheumatologist to make accurate scores for training data. In summary, these scoring-based studies can quickly determine the RA condition in the initial diagnosis but lose sensitivity in RA progression monitoring.

Scoring-based ML methods are not sensitive enough to precisely monitor RA progression. Margin detection based methods also have two main limitations: (a) fundamentally detecting the upper bone margin accurately is a perceived challenge, which is known to be affected by false edges [17], [18], [21]. (b) Margin detection based studies [9]–[22] can best achieve a pixel-level accuracy only (please see Section IV-B for more details). This can impact the timeliness of clinical decision making in RA. Although, intensity difference based JSN quantification method [22] has better sensitivity than others, but it is susceptible to imaging environments.

3) Our contributions: Original contribution of our work can be summarized as follows: (i) Describe a detection method for finger midline and joint position. (ii) Propose an image segmentation algorithm to segment joint images. (iii) Present an improved phase-only correlation method named partial image phase-only correlation (PIPOC) to measure JSN progression in the early RA stage. (iv) Automate the features listed in (i-iii). Using our method the JSN progression can be measured from a group of input sequential radiographs. (v) The proposed work can achieve sub-pixel accuracy on JSN progression measurement.

This rest of the paper is organized as follows: Section II reports a fully automatic method for the localization of the joint position, and also describes the quantification of the JSN progression in detail. In Section III, we describe our experiments; including phantom imaging, and clinical imaging. Section IV, presents the joint position detection results using clinical data and the evaluation results for both phantom imaging and clinical imaging for JSN progression quantification. Section V presents a detailed discussion with concluding remarks.

II. METHODOLOGY

The main objective of the proposed JSN quantification algorithm is to improve sensitivity, accuracy and robustness so that radiologist/rheumatologist can closely monitor the JSN progression in RA at an early stage. Ideally, the automatic quantification of JSN progression in finger joints radiographs is performed in three steps. (i) Detect and calibrate joint positions. (ii) Segment upper and lower bones of joints based on gradient information. (iii) Measure the location differences of upper and lower bones between baseline and follow-up hand radiographs respectively by using PIPOC, thus resulting in JSN quantification.

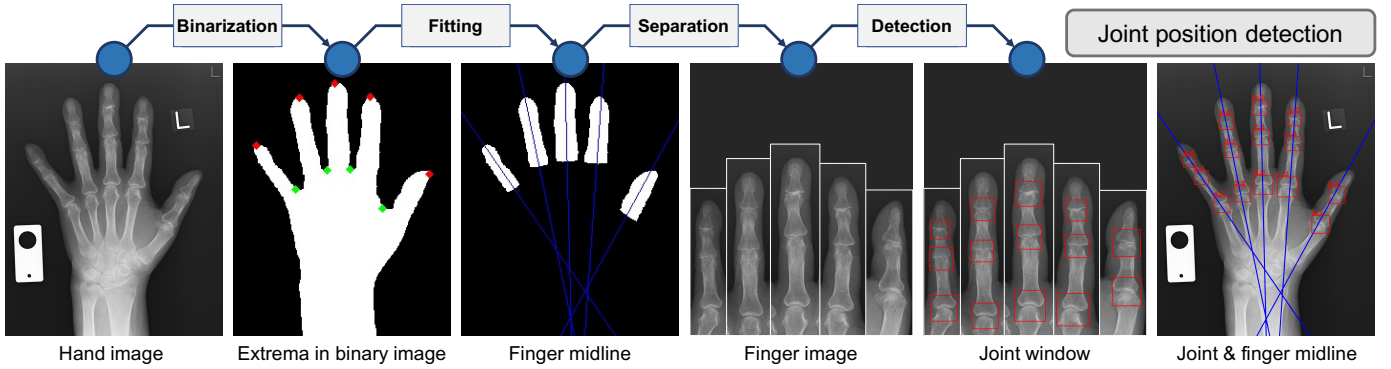


Fig. 2. Schematic overview of joint position detection. The approximate areas of fingers are obtained according to each pair of local maxima (red points) and local minima (green points) in binary image. Then, the finger midlines (blue lines) are calculated by fitting to each area. Finally, an AdaBoost based joint classifier is used to detect the joint positions (red windows).

A. Joint position detection and calibration

As shown in Fig. 2, the pipeline of joint position detection and calibration can be briefly explained as follows: (i) Obtain the approximate estimates of the finger midlines in binary image. (ii) Detect joint positions by using a ML-based joint classifier. (iii) Calibrate the relative position deviations in joint windows.

1) *Finger midline detection*: Finger position estimation can significantly reduce the potential area, thus reduces the calculation of joint detection. The scheme of finger midline detection is shown in Fig. 2, the approximate area and angle of fingers are estimated using the binary image obtained from a hand radiograph.

Given a radiograph, we binarize the X-ray using Otsu’s method [32], and smooth its margin by using morphological opening and closing [33]. We obtain the local maxima (red point) and local minima (green point) of hand margins as shown in Fig. 2. From our experiments we found that using polygonal approximation can significantly improve robustness when searching for extrema, that one could obtain using pure margin [34]. Next, the approximate area of fingers are obtained according to each pair of local maxima and minima, which can calculate the midline of each finger by fitting to each finger area based on least squares method [35].

From our experiments and analysis we found that reducing the width and height of the binary hand images to one-fifth does not significantly effect the accuracy of the finger midline detection, and this results in accelerating the detection process ($17.7\times$ faster).

2) *Joint position detection*: As shown in Fig. 2, the position, angle, and size of each finger image is obtained according to the finger midline and its area in the binary image. Then, the joint windows are detected in finger images with a joint classifier which is trained by using haar-like feature based AdaBoost [36]–[38].

3) *Joint position calibration*: We propose a low computational solution based on FIPOC to calibrate the joint position, a detailed discussion of FIPOC implementation is presented in section II-C.

The bone surface texture is frequently changing and varies when the bone is growing, and these irregular variation will cause phase dispersion in phase difference spectrum when

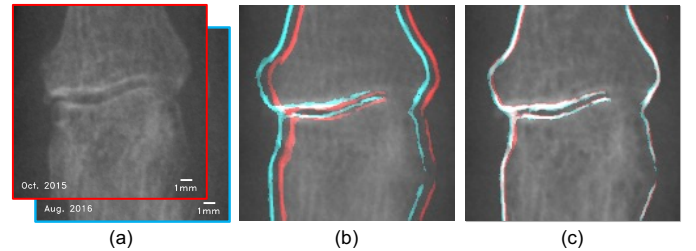


Fig. 3. Results of joint position calibration: (a) A proximal interphalangeal joint (PIP) of little finger in baseline radiograph (red border) and follow-up radiograph (cyan border). (b) The margin of PIP radiograph in (a) before position calibration (red: baseline radiograph, cyan: follow-up radiograph, white: overlap). (c) The margin information after position calibration.

using phase-only correlation method. Our experiments show that edge preserving filter can significantly reduce mismatch error of phase-only correlation, which can suppress bone surface texture information while preserving the bone margin. In our work, we preprocess the image using a median filter to calibrate position deviation [39].

As show in Fig. 3 the joint position calibration which relies on FIPOC cannot reduce the deviation with ground truth. It can limit relative position deviation between baseline and follow-up joint windows within one pixel.

B. Joint segmentation

In this stage, the upper and lower bones are segmented from the joint image, based on gradient information, so that the displacements of the upper and lower bones can be measured separately.

1) *Depth image*: The depth map is used to gauge the depth of each pixel within a given range of width. Only the vertical depth is detected in this work, because all joint images are arranged vertically. Nevertheless, the depth of any direction can be detected with a customized convolution template S_i . The detailed explanation is shown in Fig. 4.

In order to detect depth within a range of width, a height-adjustable convolution template S_i is used (i is odd) to calculate the depth of i pixels gully width. Consider an image with M pixel width and N pixel height, the convolutions of

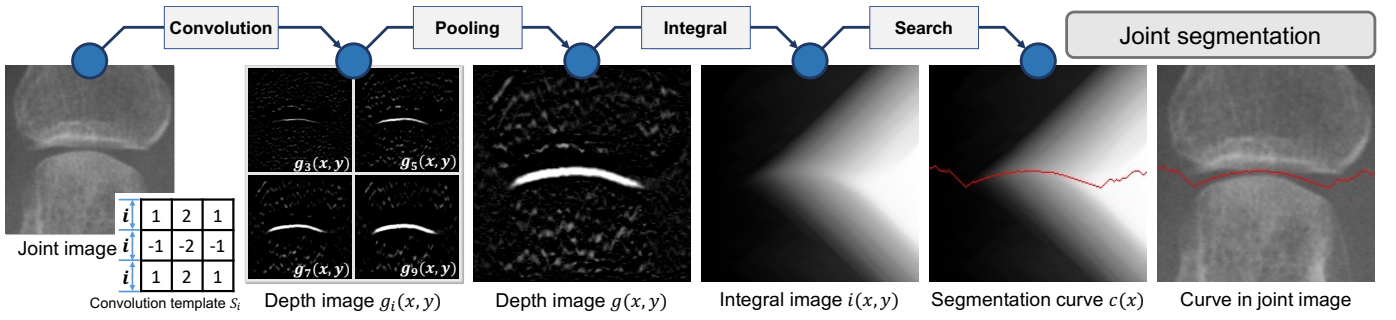


Fig. 4. Overview of joint segmentation based on gradient information. Gully depth map $g(x, y)$ is calculated to define depth feather. Independent edge filtering on the upper and lower side determines the pixel depth. Height-adjustable convolution template S_i ensures that a given range of gully can be detected. The integral image $i(x, y)$ is calculated to search the segmentation curve $c(x)$ with the maximum depth-sum.

S_{ia} and S_{ib} are as follows:

$$g_{ia}(x, y) = \sum_{k=-1}^1 \sum_{l=-(i-1)/2}^{(3i-1)/2} s_i(k, l) f(x+k, y+l) \quad (1)$$

$$g_{ib}(x, y) = \sum_{k=-1}^1 \sum_{l=-(3i-1)/2}^{(i-1)/2} s_i(k, l) f(x+k, y+l)$$

$g_{ia}(x, y)$ is the grayscale difference between the current line with the upper line, and $g_{ib}(x, y)$ is the grayscale difference between the current line with the lower line. The smaller value of $g_{ia}(x, y)$ and $g_{ib}(x, y)$ is defined as the depth, as shown in Eq. 2.

$$g_i(x, y) = \min(g_{ia}(x, y), g_{ib}(x, y)) \quad (2)$$

In this work, the range of width $[i_{min}, i_{max}]$ is defined as one to nine pixels when the spatial resolution is $0.175mm/pixel$. Next, we perform maximum pooling on depth map g_i , as show in Eq. 3.

$$g(x, y) = \max(g_{i_{min}}(x, y), \dots, g_{i_{max}}(x, y)) \quad (3)$$

As shown in Fig. 4, the depth map $g(x, y)$ corresponds to the depth information by using gradient information.

2) **Integral image:** The integral image $i(x, y)$ is an intermediate matrix, which is used to find the segmentation curve with the maximum depth-sum. It can be expressed as the local maximum in the left column plus depth map $g(x, y)$, as shown in Eq. 4.

$$i(x, y) = \begin{cases} g(x, y) & x=0 \\ \max(i(x-1, y-1), i(x-1, y), i(x-1, y+1)) + g(x, y) & x>0 \end{cases} \quad (4)$$

3) **Segmentation curve:** The segmentation curve with the maximum depth-sum can be determined from integral image $i(x, y)$ as follows. First, determine the maximum value of the rightmost column in $i(x, y)$ as the end point of the segmentation curve. Then, select the maximum of the three adjacent pixels in the left column in $i(x, y)$ as the next point of the segmentation curve until arriving at the leftmost column. The segmentation curve $c(x)$ is defined as Eq. 5. The $\arg \max_y i(x, y)$ indicates the index of the maximum value on the y axis for a given x value in a given y range.

$$c(x) = \arg \max_y i(x, y) \begin{cases} y \in [0, N-1] & x=M-1 \\ y \in [c(x+1)-1, c(x+1)+1] & x < M-1 \end{cases} \quad (5)$$

The binary matrix of upper bone area $s_0(x, y)$ and lower bone area $s_1(x, y)$ can be expressed as Eq. 6, according to the segmentation curve $c(x)$.

$$s_0(x, y) = \begin{cases} 1 & y < c(x) \\ 0 & \text{otherwise} \end{cases} \quad (6)$$

$$s_1(x, y) = \begin{cases} 1 & y > c(x) \\ 0 & \text{otherwise} \end{cases}$$

An example of finger joint segmentation is shown in Fig. 4.

C. JSN quantification by partial image phase-only correlation

The basic concept of JSN quantification by FIPOC or PIPOC can be described using the flowchart in Fig 5. Consider two images, $f(x, y)$ and $g(x, y)$, which are divided into k areas. Consider an area i , let α_i and β_i represent sub-pixel displacement from $f(x, y)$ to $g(x, y)$ in x and y directions respectively, and a binary matrix $s_i(x, y)$ that includes segmentation information. So, $g(x, y)$ can be represented as Eq. 7.

$$g(x, y) = \sum_{i=0}^k f(x - \alpha_i, y - \beta_i) * s_i(x, y) \quad (7)$$

A 2D Hanning window function is applied to input images $f(x, y)$ and $g(x, y)$ to reduce the effect of discontinuity at image border [40]. The Hanning window $w(x, y)$ can be defined as:

$$w(x, y) = \frac{1 + \cos(\frac{\pi x}{M})}{2} \frac{1 + \cos(\frac{\pi y}{N})}{2} \quad (8)$$

Let $F(u, v)$ and $G(u, v)$ denote the 2D Discrete Fourier Transforms (DFT) of the two images. Considering the properties of DFT \mathcal{F} , $F(u, v)$ and $G(u, v)$ can be expressed as Eq. 9.

$$F(u, v) = \mathcal{F}(f(x, y)w(x, y)) \quad G(u, v) = \mathcal{F}(g(x, y)w(x, y)) \quad (9)$$

Next, extract the phase component of $F(u, v)$ and $G(u, v)$, the functions are divided by the amplitude, as follows:

$$\hat{F}(u, v) = \frac{F(u, v)}{|F(u, v)|} \quad \hat{G}(u, v) = \frac{G(u, v)}{|G(u, v)|} \quad (10)$$

FIPOC will calculate the phase difference spectrum $\hat{r}(u, v)$ between $\hat{F}(u, v)$ and $\hat{G}(u, v)$ immediately (the dotted line in

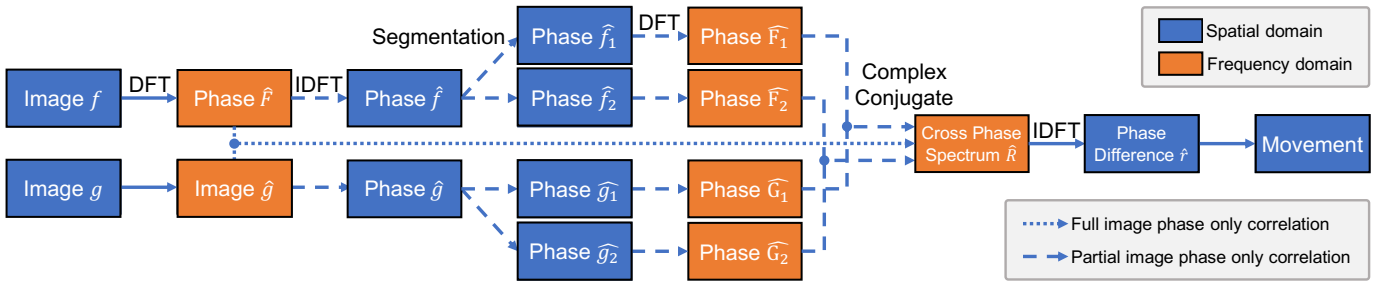


Fig. 5. A flowchart describing the sequence of operations for implementing FIPOC and PIPOC algorithms.

Fig. 5). But when the displacement of each area is different, there will be several dirac delta functions in phase difference spectrum, as show in Eq. 11.

$$\hat{r}(u, v) = \sum_{i=0}^k p_i \delta(\alpha_i, \beta_i) \quad (11)$$

Different from FIPOC, PIPOC segments the phase spectrum in spatial domain. Next, the phase spectrum $\hat{f}(x, y)$ of image $f(x, y)$ and the phase spectrum $\hat{g}(x, y)$ of image $g(x, y)$ in spatial domain are obtained by Inverse Discrete Fourier Transform (IDFT) \mathcal{F}^{-1} .

$$\hat{f}(x, y) = \mathcal{F}^{-1}(\hat{F}(u, v)) \quad \hat{g}(x, y) = \mathcal{F}^{-1}(\hat{G}(u, v)) \quad (12)$$

Segmenting area i by using segmentation matrix $s_i(x, y)$.

$$\hat{f}_i(x, y) = \hat{f}(x, y) * s_i(x, y) \quad \hat{g}_i(x, y) = \hat{g}(x, y) * s_i(x, y) \quad (13)$$

Subsequently combining DFT \mathcal{F} and Eq. 13 to develop the phase spectrum of area i in frequency domain.

$$\hat{F}_i(u, v) = \mathcal{F}(\hat{f}_i(x, y)) \quad \hat{G}_i(u, v) = \mathcal{F}(\hat{g}_i(x, y)) \quad (14)$$

The normalized cross phase spectrum $\hat{R}_i(u, v)$ of area i between $F(u, v)$ and $G(u, v)$ can be obtained respectively as given in Eq. 15. Here, $\overline{\hat{G}_i(u, v)}$ in Eq. 15 denotes the complex conjugate of $\hat{G}_i(u, v)$.

$$\hat{R}_i(u, v) = \frac{\hat{F}_i(u, v) \overline{\hat{G}_i(u, v)}}{|\hat{F}_i(u, v) \hat{G}_i(u, v)|} \quad (15)$$

Next, the phase difference spectrums $\hat{r}_i(x, y)$ of area i between the two images are obtained by IDFT \mathcal{F}^{-1} . The location of the dirac delta function δ represents the displacement between two images.

$$\begin{aligned} \hat{r}_i(x, y) &= \mathcal{F}^{-1}(\hat{R}_i(u, v)) \\ &= \delta(\alpha_i, \beta_i) \end{aligned} \quad (16)$$

In case of Fourier Transform, the location of the peak of dirac delta function δ in the phase difference spectrum $\hat{r}_i(x, y)$ can be determined according to the maximum peak.

$$(\alpha_i', \beta_i') = \arg \max_{(x, y)} \hat{r}_i(x, y) \quad (17)$$

Consider the DFT, the least-square fitting method employed to estimate displacement (α_i, β_i) around the maximum peak (α_i', β_i') . Since the δ function has a very sharp peak, limited number of data points 5×5 are used to fit δ function [40] in this work. Thus, the JSN_{fg} between image $f(x, y)$ and

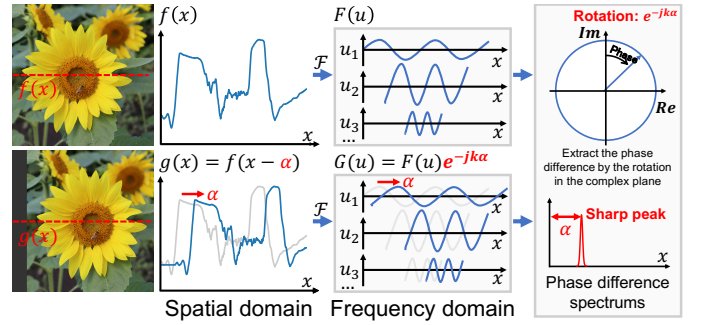


Fig. 6. Principles of FIPOC. Consider two signals $f(x)$ and $g(x)$ with α displacement. Since each wave has the same phase difference, the displacement can be measured by the location of dirac delta function in the phase difference spectrum.

image $g(x, y)$ can be quantified according to the displacement difference between upper bone area $s_0(x, y)$ and lower bone area $s_1(x, y)$, as show below.

$$\text{JSN}_{fg} = \beta_0 - \beta_1 \quad (18)$$

D. PIPOC and FIPOC

Earlier we had proposed a JSN quantification method [23], [24], which is based on full image phase-only correlation (FIPOC) [40]–[43]. FIPOC is a well-known method for image registration, it can estimate the relative displacement between two images and it relies on the frequency domain analysis. Figure 6 shows a one dimension diagram of FIPOC, it has sub-pixel level accuracy and error range within 0.01 pixel when measured on a set of $200 \text{ pixel} \times 200 \text{ pixel}$ images [40], and the accuracy improves with higher image resolution.

FIPOC can calculate displacement between two images by measuring the phase difference in frequency domain. However, it has a limitation when there are multiple areas with different displacements. Each local area would have a corresponding independent dirac delta function in phase difference spectrum. The precise position of each dirac delta function can be obtained if and only if the displacement differences between multiple areas are large enough (about 3 pixel [44]). Otherwise, dirac delta functions in phase difference spectrum will be affected and even overlap.

In our conference paper [23], we segmented joint images in spatial domain and fill vacant space by using image in-painting algorithm [45] to solve the overlapping issue. Thus, the displacements of upper and lower bones could be quantified

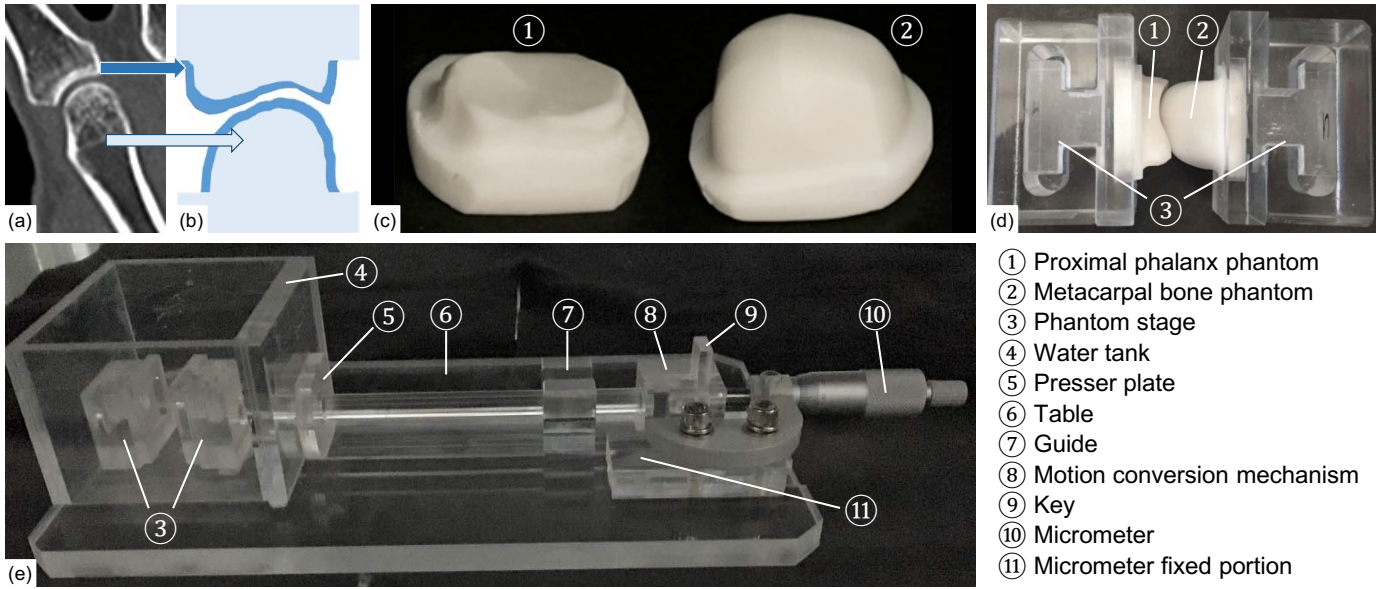


Fig. 7. A MCP joint-shaped two-layer phantom design and phantom imaging environment. (a) A MCP joint in radiographic clinical imaging. (b) A diagram of two-layer structure bone (dark blue: Bone cortex, light blue: Cancellous bone). (c) A set of MCP joint-shaped two-layer phantom. (d) The phantom joint connect with the attaching portion. (e) The phantom imaging environment.

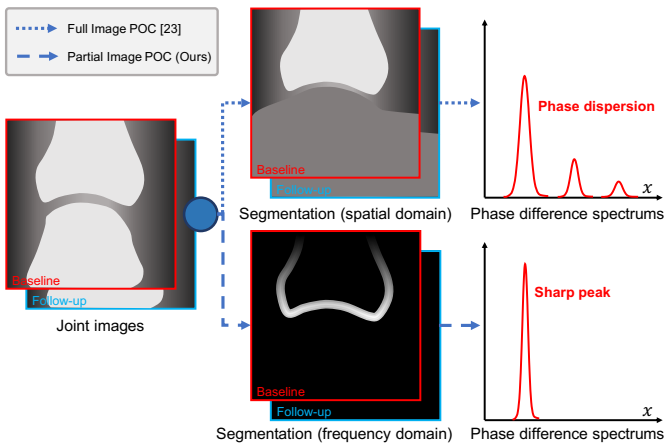


Fig. 8. Difference between FIPOC and PIPOC for JSN measurement. FIPOC-based JSN measurement requires the segmentation of upper and lower bone, and in-painting algorithm is used to fill vacant space, this could lead to phase dispersion as shown above. In this work (PIPOC) we obtain a sharper delta function by quantifying the displacement by segmenting joint image in the phase spectrum of the frequency domain.

from independent bone images based on FIPOC respectively. But some non-existent phase features may be generated which could increase error and even mismatches, as shown in Fig. 8. To avoid the impact from in-painting algorithm, the partial image phase-only correlation (PIPOC) is proposed in this work. The basic idea of PIPOC is to determine the location of each dirac delta functions by segmenting the phase spectrum. Compared to FIPOC combined image in-painting, PIPOC can further improve the accuracy and robustness of JSN quantification, by eliminating the impact of image in-painting algorithm.

III. MATERIALS

Imaging phantom based experiments were studied to evaluate our algorithm's performance. From our experiments we observed that the manually labeled JSW has pixel level mean error, and it is discussed in Section IV-B.1. We prepared phantom images with ground truth to evaluate our algorithm in terms of absolute error. Additionally, our algorithm's quality performance was also evaluated using clinical data.

A. Phantom imaging

1) *Phantom design*: A phalanx-shaped phantom was produced using vacuum-sintered bodies of a novel apatite called Titanium medical apatite (TMA) [46]. The chemical formula of TMA is $Ca_{10}(PO_4)_6 \cdot TiO_2 \cdot (OH)_2 \cdot nH_2O$. TMA powder was kneaded with distilled water, and solid cylinders of compacted TMA were formed by compression molding at $10MPa$. TMA was vacuum sintered using a resistance furnace at about $10^{-3}Pa$.

Using TMA to design imaging phantom has the following advantages: (1) The CT value of phantom in radiographs can be easily modified by changing the ratio of TMA and adhesive. (2) TMA bodies are easy to process and model with a 3D-modeling machine or a lathe. (3) TMA vacuum-sintered bodies has a density of approximately $2300kg/m^3$ (corresponding to that of a compact bone or a tooth).

The phantom used in our experiment is a two-layer TMA vacuum-sintered body to simulate the X-ray absorption coefficient (CT value) of bone cortex and cancellous bone. The diagram of the two-layered bone is shown in Fig. 7 (a) and (b). The phantom mimics MCP joint, proximal phalanx, and the metacarpal bone. The assembled phantoms are shown in Fig. 7 (c). The important properties of our phantom bones are given in Table I [22], [46].

TABLE I
PHANTOM DESIGN PREPARATION

	Bone cortex	Cancellous bone
TMA : adhesive	1:1.2	1:5
Particle Size (μm)	107 ~ 250	107 ~ 250
Temperature (K)	1370	1370

TABLE II
X-RAY IMAGING CONFIGURATION PARAMETERS

	Phantom	Clinical
Tube voltage (kV)	50	42
Tube current (mA)	100	100
Exposure time (mSec)	20	20
Source to image (cm)	100	100

2) *Imaging environment*: The phantom joint was mounted on to the stage as shown in Fig. 7 (d). The phantom stage was connected to a micrometer, and thereby the JSW of phantom could be easily adjusted using the micrometer controls. The JSW range is up to 13mm , and has a minimum scale of 0.01mm . There is substantial evidence that JSW has a close relationship with age and sex in healthy populations [7], [47]. In addition, RA is more frequent in females who are between 30 and 50 years of age, and their JSW is around 1.70mm [7], [47]. In our work, the JSW standard of phantom was set as 1.70mm . Following two sets of phantom images with different specifications were provided. (i) JSW range: 1.20mm - 2.20mm , increment step size: 0.10mm (ii) JSW range: 1.65mm - 1.75mm , increment step size: 0.01mm .

Considering that in clinical data, the X-ray beam can be attenuated by the tissue, these attenuations are displayed as noise in the radiography. In related phantom studies, water is usually used to simulate the noise generated by the beam attenuation in the tissue [48], [49]. In our experiment, the phalanx-shaped phantom was mounted on the stage as shown in Fig. 7 (d), and placed in a tank. We can image the phantom with low noise when the tank is filled with air, or filled with distilled water which has an X-ray absorbing properties similar to normal tissue. Our experimental phantom imaging setup is shown in Fig. 7 (e). The X-ray imaging equipment used in our experiment is: digital radiography (*FUJIFILM DR CALNEO Smart C47*, Fujifilm Corporation, Tokyo, Japan), and its parameters are given in Table II. The spatial resolution used in this phantom study is $0.15\text{mm}/\text{pixel}$.

B. Clinical dataset

1) *Study population*: For clinical assessment, we prepared dataset from *Sagawa Akira Rheumatology Clinic* (Sapporo, Japan), *Sapporo City General Hospital* (Sapporo, Japan) and *Hokkaido Medical Center for Rheumatic Diseases* (Sapporo, Japan). This dataset contains 1120 hand posteroanterior projection (PA) radiographs from patients in the early RA stage. All images were used in the joint position detection experiments. Considering that several images were required to evaluate our work when calculating standard deviation. Thus, images of patients who were radiographed at least three times were retained, which contains 549 hand PA radiographs of 77 RA

TABLE III
PATIENT INFORMATION IN THE CLINICAL DATASET

	Mean \pm SD	Range
Age at enrollment (year)	55.83 ± 13.86	$20.68 \sim 88.00$
Number of Photography*	4.30 ± 2.54	$3 \sim 17$
Treatment Time (year)	4.01 ± 3.43	$0.88 \sim 12.10$

* Patients did two-handed or one-handed radiographic imaging.

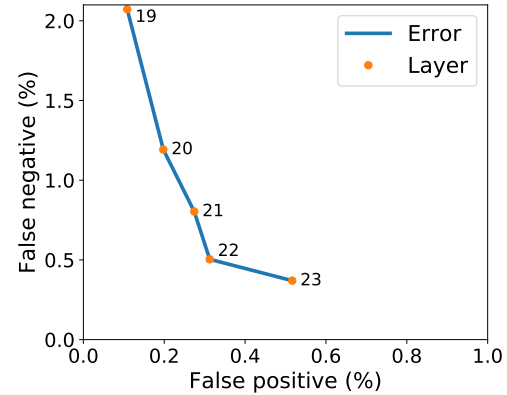


Fig. 9. The variation in false positive and false negative ratios with the increase of the cascade layers.

patients out of which 88.0% are female. Detailed patients information are summarized in Table III (please note, the gender and age information of a small number of patients were not included upon patient request).

This study was conducted in accordance with the guidelines of the Declaration of Helsinki and approved by the Ethics Committee of the Faculty of Health Sciences, Hokkaido University (approval number: 19 – 46).

2) *Imaging environment*: The radiographic imaging device used in our clinical study is *DR-155HS2-5* from *Hitachi* Corporation, with 1.5mm X-ray aluminum filter thickness. The centering point of the X-ray beam was the MCP joint of the middle finger. Digital imaging and communications in medicine (DICOM) standard was used in managing our radiographic dataset, and the image resolution is 2010×1490 , and a $0.175 \times 0.175\text{mm}$ pixel size at 12 bit depth. For detailed imaging parameter descriptions, please refer to Table II.

IV. EXPERIMENTS AND DISCUSSION

A. Joint position detection

The results of joint location detection are shown in Fig. 9, the false negative of classifier decreases gradually with the increase of the cascade layers, and false positive gradually increase after 22 levels. We selected the 22-layer classifier for joint position detection, which has a false negative ratio and a false positive ratio of 0.31% and 0.50% respectively. The performance on each joint is shown in the Table V. From this table, we can observe that false positives occurred mainly in the carpometacarpal (CMC) joint of the thumb, which is the joint that most closely resembles the target joints in a hand radiograph. And false negative appeared mainly in the thumb, especially the interphalangeal (IP) joint. In our opinion, the main reason for this situation is that the

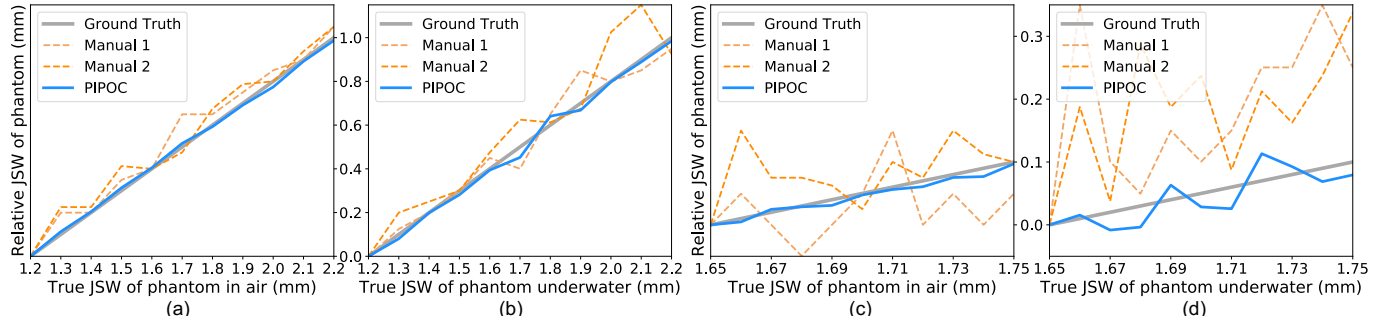


Fig. 10. The measurement result of PIPOC and manual when using phantom images. Blue lines are the relative JSW of each image to the first image obtained by PIPOC. Orange dot lines are the difference of manually measured JSW between every image and the first image. The true JSW of phantom is from $1.20mm$ to $2.20mm$ at increments of $0.10mm$ in sub-figure (a) and (b). And it is from $1.65mm$ to $1.75mm$ at increments of $0.01mm$ in sub-figure (c) and (d). The phantom of sub-figure (a) and (c) is placed in air. And the phantom of sub-figure (b) and (d) is placed in distilled water.

TABLE IV

THE PERFORMANCE ANALYSIS IN MILLIMETER FOR PIPOC AND MANUAL MEASUREMENT WHEN USING PHANTOM IMAGES

	Mean Error						Root-Mean-Square Deviation					
	Air			Water			Air			Water		
	Fig.10 (a)	Fig.10 (c)	Average	Fig.10 (b)	Fig.10 (d)	Average	Fig.10 (a)	Fig.10 (c)	Average	Fig.10 (b)	Fig.10 (d)	Average
Manual 1	0.0509	0.0620	0.0565	0.0727	0.1196	0.0961	0.0665	0.0758	0.0711	0.0923	0.1450	0.1186
Manual 2	0.0595	0.0497	0.0546	0.1186	0.1034	0.1110	0.0709	0.0632	0.0671	0.1440	0.1237	0.1339
Mean of Manual	0.0552	0.0559	0.0555	0.0957	0.1115	0.1036	0.0687	0.0695	0.0691	0.1182	0.1343	0.1263
PIPOC (Ours)	0.0193	0.0066	0.0130	0.0251	0.0200	0.0226	0.0220	0.0081	0.0150	0.0303	0.0245	0.0274
FIPOC [23]	0.0400	-	0.0400	-	-	-	-	-	-	-	-	-

TABLE V

FALSE NEGATIVE AND FALSE POSITIVE COUNTS AND RATIOS OF JOINT LOCATION DETECTION

	False Negative				False positive	
	IP	DIP	PIP	MCP	CMC	Others
Thumb	24	N/A	N/A	5	63	2
Index	N/A	0	2	0	0	7
Middle	N/A	1	1	0	0	2
Ring	N/A	2	0	2	0	4
Small	N/A	11	1	0	0	1
Overall	24 (2.14%)	14 (0.31%)	4 (0.09%)	7 (0.16%)	63	16

* IP: Interphalangeal joint. DIP: Distal interphalangeal joint.
PIP: Proximal interphalangeal joint. CMC: Carpometacarpal joint.

radiographic angle of the thumb is different from other fingers, resulting a difference in radiography. Differentiation of the joint position detection on the thumb may be effective in improving detection accuracy.

B. JSN quantification

1) *Phantom data*: Phantom images with ground truth were used in this experiment to calculate the absolute error of PIPOC, and to compare it with manual measurement. Manual measurement was done once with care by one radiologist and one radiological technologist after substantial training. They did not know the ground truth of the out-of-order phantom images. They were asked to determine the center of the upper phantom by drawing straight lines horizontally connecting both ends of the phantom base, then a straight line was drawn from the center vertically, and the JSW overlapping the straight line was measured.

Consider a set with n phantom images. The mean error E and root-mean-square deviation (RMSD) can be defined as:

$$E = \frac{2}{n(n-1)} \sum_{f=2}^n \left(\sum_{g=1}^{f-1} |JSN_{fg} - T_{fg}| \right) \quad (19)$$

$$RMSD = \sqrt{\frac{2}{n(n-1)} \sum_{f=2}^n \left(\sum_{g=1}^{f-1} (JSN_{fg} - T_{fg})^2 \right)} \quad (20)$$

Where JSN_{fg} is the measured JSN between image f and image g by using PIPOC or manual measurement. And T_{fg} represents the ground truth.

Figure 10 and Table IV presents the measurement result of phantom sets. The manual measurement result of the radiologist and the radiological technologist showed high similarity in terms of mean error and RMSD in multiple phantom data sets. The mean error of manual measurements is about $0.0555mm$ ($0.37pixel$) in low noise environment (air sets), and $0.1036mm$ ($0.69pixel$) in high noise environment (water sets). This shows that visual measurement also can be greatly affected by the noise. On the other hand, this also indicates the manually annotated data have sub-pixel level mean error. Hence, the manually annotated ground truth may result in sub-pixel level deviation in algorithm evaluation of other works.

In paper [23], only one phantom set (environment: air, JSW range: $1.20mm$ - $2.20mm$, increment step size: $0.10mm$) is used in experiment. The mean error of FIPOC is slightly lower than manual measurement. When compared to FIPOC, PIPOC can further improve the accuracy and robustness in JSN quantification, by eliminating the impact of image inpainting algorithm. As show in Table IV, our work only has a 11.9% to 35.0% mean error, and a 11.7% to 32.0% RMSD when compare to manual measurement. This illustrates

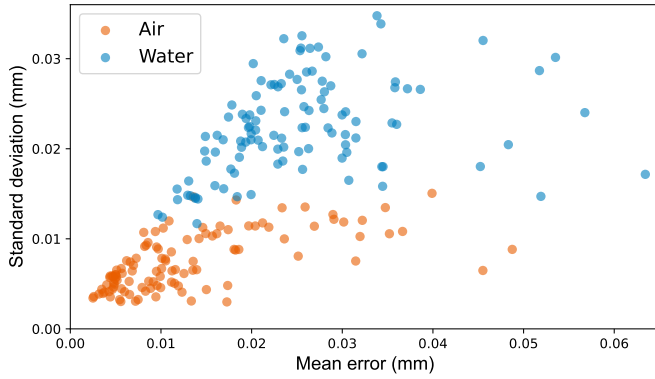


Fig. 11. The mean error E and the standard deviation σ of all sets of JSN in phantom data.

the improved performance of JSN quantification when using phantom datasets.

In related works, the ground truth of joint space is usually measured by the radiologist or the rheumatologist manually. But as discussed above, manual measurement also have sub-pixel level mean error. Thus, manually measured ground truth may result in sub-pixel deviation in algorithm evaluation. This deviation is negligible when evaluating the algorithm on a pixel scale. But it can be inaccurate on a sub-pixel scale.

To the best of our knowledge there are no published algorithms/methods which can compute ground truth RA joint space with sub-pixel accuracy. We propose to use the standard deviation σ of multiple measurements to demonstrate the reliability of PIPOC without ground truth. The definition of standard deviation can be described as follows.

In case of three images f , g and k , the JSN_{fg-k} between image f and image g can be indirectly calculated by introducing intermediate image k . As show in Eq. 21.

$$\text{JSN}_{fg-k} = \text{JSN}_{fk} + \text{JSN}_{kg} \quad (21)$$

Considering a set of images, the $\overline{\text{JSN}_{fg}}$ can be obtained by taking the average of multiple measurements.

$$\overline{\text{JSN}_{fg}} = \frac{1}{n} \sum_{k=1}^n \text{JSN}_{fg-k} \quad (22)$$

So, the standard deviation σ of JSN_{fg} is defined as Eq. 23.

$$\sigma_{fg} = \sqrt{\frac{1}{n} \sum_{k=1}^n (\text{JSN}_{fg-k} - \overline{\text{JSN}_{fg}})^2} \quad (23)$$

The standard deviation σ_{fg} represents a dispersion of a set of JSN_{fg-k} ($k \in [1, n]$). According to our experiments when using phantom datasets, the standard deviation σ and the mean error E has a high positive correlation, as show in Fig. 11. The Pearson correlation coefficient between σ and E is 0.641 (count: 220, p -value: $< .001$). For the above reason, and the most important advantage that the standard deviation σ not relying on the ground truth, we used it to measure the performance of our work in clinical databases. In addition, we also found that noise in radiography due to beam attenuation in tissue can greatly affects the accuracy of measurements especially in terms of standard deviation.

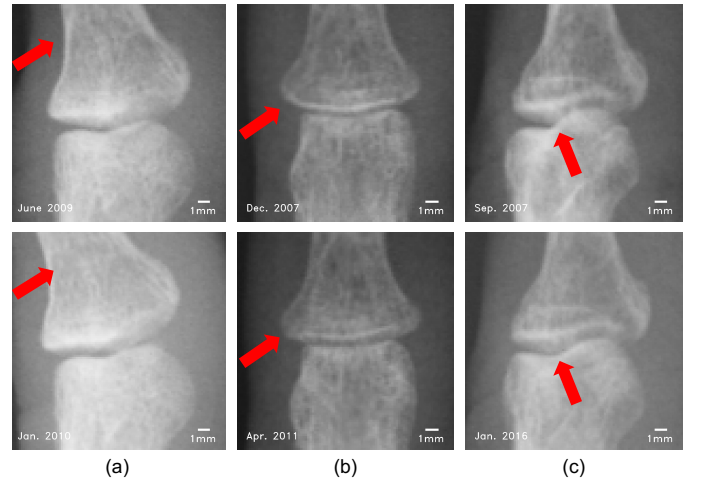


Fig. 12. Joints with mismatched registration. (a) Inconsistent joint angle. (b) Bended finger. (c) Inconsistent projection angle.

TABLE VI

THE MEAN STANDARD DEVIATION IN MILLIMETER AND THE MISMATCHING RATIOS FOR PIPOC

	Clinical Data				Phantom Data	
	IP	DIP	PIP	MCP	Air	Water
Thumb	0.093(7.2%)	N/A	N/A	0.078(4.5%)	-	-
Index	N/A	0.047(4.0%)	0.065(5.2%)	0.051(1.6%)	-	-
Middle	N/A	0.055(5.8%)	0.061(3.4%)	0.057(4.3%)	-	-
Ring	N/A	0.029(4.1%)	0.033(1.8%)	0.023(1.8%)	-	-
Small	N/A	0.044(5.9%)	0.053(3.7%)	0.038(2.0%)	-	-
Overall	0.093(7.2%)	0.044(5.0%)	0.053(3.5%)	0.050(2.8%)	0.007	0.025

2) *Clinical data*: 549 hand PA radiographs have been analyzed in this subsection. Compared to phantom data, clinical data face additional challenges. The major challenge in this work is the uncertainty of hand posture, different hand postures can present differentiated bone contours.

According to our experiments, changes in bone contours can affects the accuracy of JSN quantification. Here, we showcase (see Fig. 12) majority of mismatch bone contour cases. The most frequent reason is the inconsistent angle between the upper and lower bones of joint, as show in Fig. 12 (a). This mainly occurs on IP and MCP joints. PIPOC has high accuracy for translation detection, but weak resistance to rotation. Another important reason of mismatched registration is the bending of the fingers, which appears on DIP and PIP joints, for an example see Fig. 12 (b). Finger bending can result in the changes of the far margin appearance of upper bone. Besides, inconsistent projection angle also can be the reason, see Fig. 12 (c). Most of the time it happens only on the IP joint, which is caused by inconsistent joint position or thumb roll. The individuated finger movements differ greatly as studied in [50]. Movements of the thumb, index finger, and little finger typically were more highly individuated than were movements of the middle or ring fingers. The angular motion tended to be greatest at the PIP joint of each digit [50]. It is worth noting that, the flexibility of joint and standard deviation express high positive correlation (refer Table VI).

In summary, the hand posture should be consistent and avoid bending of the fingers, especially the thumb when using our

TABLE VII

COMPARISON WITH RELATED WORKS. MEAN ERROR AND STANDARD DEVIATION IN MILLIMETER. NUMBERS IN BRACES INDICATE THE CORRESPONDING PERCENTAGE OF THE GROUND TRUTH VALUE FOR THE RESPECTIVE JOINT.

Method	Dataset	Resolution (mm/pixel)	Mean Error				Standard Deviation				
			DIP	PIP	MCP	Overall	DIP	PIP	MCP	Overall	
Neural Network [25]	AAPM'99	240 radiographs	0.1	0.118	0.071	0.091	0.093	-	-	-	-
Active Shape Models [10]	TMI'08	160 MCP joints	0.0846	-	-	0.283(16.1%)	0.283(16.1%)	-	-	0.080(4.5%)	0.080(4.5%)
Edge Detection [21]	TBME'15	104 radiographs	0.1	(5.8%)	(7.2%)	(7.1%)	(6.8%)	(4.8%)	(5.3%)	(4.4%)	(4.8%)
Full Image POC [23]	ISBI'19	Phantom data	0.15	-	-	0.040	0.040	-	-	-	-
Manual Measurement	-	Phantom data	0.15	-	-	0.056	0.056	-	-	-	-
Partial Image POC (Ours)	-	Phantom data	0.15	-	-	0.013	0.013	-	-	0.007	0.007
Partial Image POC (Ours)	-	549 radiographs	0.175	-	-	-	-	0.044	0.053	0.050	0.049

work for JSN quantification. Thus, we strongly recommend that using guide lines lines to standardize hand posture in taking radiography, this simple step can greatly improve the accuracy of PIPOC.

3) *Comparison with related works*: Table VII compares our work with previous JSW/JSN quantification works. In paper [25], they only used RMSD instead of mean error to evaluate the accuracy of their work, so we standardized the error metric accordingly. Considering that the error should conform to a Gaussian distribution, the mean error and RMSD can be transformed by Eq. 24.

$$E = \int_{-\infty}^{+\infty} |x| \cdot \frac{1}{\sqrt{2\pi} \cdot \text{RMSD}} e^{-\frac{x^2}{2 \cdot \text{RMSD}^2}} dx \quad (24)$$

$$= \sqrt{\frac{2}{\pi}} \cdot \text{RMSD}$$

In paper [21], authors only give the corresponding percentage of the error to the ground truth. Considering the JSW of MCP is around 1.70mm [7], [47], the mean error of MCP in millimeter is around 0.121. It is noteworthy that, papers [10], [21], [25] used manual measurement results as ground truth. As discussed above and in Table VII, manual measurement has an error about 0.056mm (low noise) / 0.104mm (high noise) when using phantom data (spatial resolution: 0.15mm/pixel). Although this value can decrease with higher spatial resolution, it is undeniable that in these works which employ manual measurement as the ground truth, the mean error may have a deviation.

The calculation procedure of standard deviation in paper [10] is different from ours. They measured JSW of each joint 10 times with varying clipping of the entire radiograph. The standard deviation quantified the uncertainty of measuring a radiograph. In our work, an intermediate radiograph is introduced in standard deviation calculation. The JSN progression between the two radiographs and the intermediate image is calculated respectively, thus, the standard deviation can be obtained by changing the intermediate image. When using the standard deviation calculation method given in paper [10], we measured a lower standard deviation (DIP: 0.0099mm, PIP: 0.0095mm, MCP: 0.0061mm). These standard deviations do not include mismatched data, the mismatching ratios are shown in Table VI).

We can observe from Table VII that even though the spatial resolution of our work is poorer than those in the related works, our mean error and the standard deviation are significantly lower.

V. CONCLUSION AND FUTURE WORKS

Our work aims for computer-aided diagnosis of rheumatoid arthritis through automatic quantification of the joint space narrowing (JSN). We proposed an automatic algorithm pipeline, including joint position detection, joint segmentation and joint space narrowing quantification based on partial image phase-only correlation (PIPOC). From our experiments we observe highest JSN quantification accuracy when compared to similar algorithms.

Additionally, our work can measure the displacements of upper and lower bones with sub-pixel accuracy. The measured mean error of our algorithm is in range of 11.9% - 35.0% in comparison to manual measurements using multiple phantom datasets, with a standard deviation of 0.0519mm when using clinical dataset. This algorithm greatly improves the accuracy and sensitivity of JSN quantification, which might help radiologists/rheumatologists to make more timely judgments on diagnosis and prognosis in rheumatoid arthritis patients.

Currently, machine learning is applied to difficult tasks, and we anticipate future studies in this direction. To address the posture (finger movement) related constraints and inconsistent joint angle which is likely to result in mismatched registration. We can quantify JSN by machine learning using the image features extracted by our work, this can improve the overall performance of the algorithm.

VI. ACKNOWLEDGMENTS

The authors would like to sincerely thank Akira Sagawa, MD, Sagawa Akira Rheumatology Clinic (Sapporo, Japan), Masaya Mukai, MD, Sapporo City General Hospital (Sapporo, Japan) and kazuhide Tanimura, MD, Hokkaido Medical Center for Rheumatic Diseases (Sapporo, Japan) for image data preparation.

REFERENCES

- [1] J. J. Cush, A. Kavanaugh, and M. E. Weinblatt, *Rheumatoid arthritis: early diagnosis and treatment*. Professional Communications, 2010.
- [2] A. Young, J. Dixey, N. Cox, P. Davies, J. Devlin, P. Emery, S. Gallivan, A. Gough, D. James, P. Prouse *et al.*, "How does functional disability in early rheumatoid arthritis (ra) affect patients and their lives? results of 5 years of follow-up in 732 patients from the early ra study (eras)," *Rheumatology*, vol. 39, no. 6, pp. 603–611, 2000.
- [3] K. G. Saag, G. G. Teng, N. M. Patkar, J. Anuntiyo, C. Finney, J. R. Curtis, H. E. Paulus, A. Mudano, M. Pisu, M. Elkins-Melton *et al.*, "American college of rheumatology 2008 recommendations for the use of nonbiologic and biologic disease-modifying antirheumatic drugs in rheumatoid arthritis," *Arthritis Care & Research: Official Journal of the American College of Rheumatology*, vol. 59, no. 6, pp. 762–784, 2008.

- [4] V. Majithia and S. A. Geraci, "Rheumatoid arthritis: diagnosis and management," *The American journal of medicine*, vol. 120, no. 11, pp. 936–939, 2007.
- [5] D. Van der Heijde, "How to read radiographs according to the sharp/van der heijde method," *The Journal of rheumatology*, vol. 27, no. 1, p. 261, 2000.
- [6] S. A. Bergstra, J. A. Van Der Pol, N. Riyazi, Y. P. Goekoop-Ruiterman, P. J. Kerstens, W. Lems, T. W. Huizinga, and C. F. Allaart, "Earlier is better when treating rheumatoid arthritis: but can we detect a window of opportunity?" *RMD open*, vol. 6, no. 1, p. e001242, 2020.
- [7] T. K. Kvien, T. Uhlig, S. ØDEGÅRD, and M. S. Heiberg, "Epidemiological aspects of rheumatoid arthritis: the sex ratio," *Annals of the New York Academy of Sciences*, vol. 1069, no. 1, pp. 212–222, 2006.
- [8] T. Shimizu, A. Cruz, M. Tanaka, K. Mamoto, V. Podoia, A. J. Burghardt, U. Heilmeyer, T. M. Link, J. Graf, J. B. Imboden *et al.*, "Structural changes over a short period are associated with functional assessments in rheumatoid arthritis," *The Journal of rheumatology*, vol. 46, no. 7, pp. 676–684, 2019.
- [9] P. Peloschek, G. Langs, M. Weber, J. Sailer, M. Reissegger, H. Imhof, H. Bischof, and F. Kainberger, "An automatic model-based system for joint space measurements on hand radiographs: initial experience," *Radiology*, vol. 245, no. 3, pp. 855–862, 2007.
- [10] G. Langs, P. Peloschek, H. Bischof, and F. Kainberger, "Automatic quantification of joint space narrowing and erosions in rheumatoid arthritis," *IEEE transactions on medical imaging*, vol. 28, no. 1, pp. 151–164, 2008.
- [11] T. Hirano, M. Nishide, N. Nonaka, J. Seit, K. Ebina, K. Sakurada, and A. Kumanogoh, "Development and validation of a deep-learning model for scoring of radiographic finger joint destruction in rheumatoid arthritis," *Rheumatology advances in practice*, vol. 3, no. 2, p. rkz047, 2019.
- [12] K. Üreten, H. Erbay, and H. H. Maraş, "Detection of rheumatoid arthritis from hand radiographs using a convolutional neural network," *Clinical rheumatology*, vol. 39, no. 4, pp. 969–974, 2020.
- [13] K. Maziarz, A. Krason, and Z. Wojna, "Deep learning for rheumatoid arthritis: Joint detection and damage scoring in x-rays," *arXiv preprint arXiv:2104.13915*, 2021.
- [14] K. Morita, P. Chan, M. Nii, N. Nakagawa, and S. Kobashi, "Finger joint detection method for the automatic estimation of rheumatoid arthritis progression using machine learning," in *2018 IEEE International Conference on Systems, Man, and Cybernetics (SMC)*. IEEE, 2018, pp. 1315–1320.
- [15] K. Nakatsu, K. Morita, N. Yagi, and S. Kobashi, "Finger joint detection method in hand x-ray radiograph images using statistical shape model and support vector machine," in *2020 International Symposium on Community-centric Systems (Ccs)*. IEEE, 2020, pp. 1–5.
- [16] J. Duryea, Y. Jiang, M. Zakharevich, and H. Genant, "Neural network based algorithm to quantify joint space width in joints of the hand for arthritis assessment," *Medical physics*, vol. 27, no. 5, pp. 1185–1194, 2000.
- [17] J. Angwin, G. Heald, A. Lloyd, K. Howland, M. Davy, and M. F. James, "Reliability and sensitivity of joint space measurements in hand radiographs using computerized image analysis," *The Journal of rheumatology*, vol. 28, no. 8, pp. 1825–1836, 2001.
- [18] R. Van't Klooster, E. Hendriks, I. Watt, M. Kloppenburg, J. Reiber, and B. Stoel, "Automatic quantification of osteoarthritis in hand radiographs: validation of a new method to measure joint space width," *Osteoarthritis and Cartilage*, vol. 16, no. 1, pp. 18–25, 2008.
- [19] A. Bielecki, M. Korkosz, and B. Zieliński, "Hand radiographs preprocessing, image representation in the finger regions and joint space width measurements for image interpretation," *Pattern Recognition*, vol. 41, no. 12, pp. 3786–3798, 2008.
- [20] B. Zieliński, "Hand radiograph analysis and joint space location improvement for image interpretation," *Schedae Informaticae*, vol. 17, 2009.
- [21] Y. Huo, K. L. Vincken, D. van der Heijde, M. J. De Hair, F. P. Lafeber, and M. A. Viergever, "Automatic quantification of radiographic finger joint space width of patients with early rheumatoid arthritis," *IEEE Transactions on Biomedical Engineering*, vol. 63, no. 10, pp. 2177–2186, 2015.
- [22] K. Kato, N. Yasojima, K. Tamura, S. Ichikawa, K. Sutherland, M. Kato, J. Fukae, K. Tanimura, Y. Tanaka, T. Okino *et al.*, "Detection of fine radiographic progression in finger joint space narrowing beyond human eyes: Phantom experiment and clinical study with rheumatoid arthritis patients," *Scientific reports*, vol. 9, no. 1, pp. 1–10, 2019.
- [23] Y. Ou, P. Ambalathankandy, T. Shimada, T. Kamishima, and M. Ikebe, "Automatic radiographic quantification of joint space narrowing progression in rheumatoid arthritis using poc," in *2019 IEEE 16th International Symposium on Biomedical Imaging (ISBI 2019)*. IEEE, 2019, pp. 1183–1187.
- [24] A. Taguchi, S. Shishido, Y. Ou, M. Ikebe, T. Zeng, W. Fang, K. Murakami, T. Ueda, N. Yasojima, K. Sato *et al.*, "Quantification of joint space width difference on radiography via phase-only correlation (poc) analysis: a phantom study comparing with various tomographical modalities using conventional margin-contouring," *Journal of Digital Imaging*, vol. 34, no. 1, pp. 96–104, 2021.
- [25] J. Duryea, Y. Jiang, P. Countryman, and H. Genant, "Automated algorithm for the identification of joint space and phalanx margin locations on digitized hand radiographs," *Medical Physics*, vol. 26, no. 3, pp. 453–461, 1999.
- [26] M. N. Wernick, Y. Yang, J. G. Brankov, G. Yourganov, and S. C. Strother, "Machine learning in medical imaging," *IEEE signal processing magazine*, vol. 27, no. 4, pp. 25–38, 2010.
- [27] O. Ronneberger, P. Fischer, and T. Brox, "U-net: Convolutional networks for biomedical image segmentation," in *International Conference on Medical image computing and computer-assisted intervention*. Springer, 2015, pp. 234–241.
- [28] N. Asiri, M. Hussain, F. Al Adel, and N. Alzaidi, "Deep learning based computer-aided diagnosis systems for diabetic retinopathy: A survey," *Artificial intelligence in medicine*, vol. 99, p. 101701, 2019.
- [29] G. Haskins, U. Kruger, and P. Yan, "Deep learning in medical image registration: a survey," *Machine Vision and Applications*, vol. 31, no. 1, pp. 1–18, 2020.
- [30] B. J. Erickson, P. Korfiatis, Z. Akkus, and T. L. Kline, "Machine learning for medical imaging," *Radiographics*, vol. 37, no. 2, pp. 505–515, 2017.
- [31] S. Lee, M. Choi, H.-s. Choi, M. S. Park, and S. Yoon, "Fingernet: Deep learning-based robust finger joint detection from radiographs," in *2015 IEEE Biomedical Circuits and Systems Conference (BioCAS)*. IEEE, 2015, pp. 1–4.
- [32] N. Otsu, "A threshold selection method from gray-level histograms," *IEEE transactions on systems, man, and cybernetics*, vol. 9, no. 1, pp. 62–66, 1979.
- [33] R. M. Haralick, S. R. Sternberg, and X. Zhuang, "Image analysis using mathematical morphology," *IEEE transactions on pattern analysis and machine intelligence*, no. 4, pp. 532–550, 1987.
- [34] J. Sklansky and V. Gonzalez, "Fast polygonal approximation of digitized curves," *Pattern Recognition*, vol. 12, no. 5, pp. 327–331, 1980.
- [35] D. York, "Least squares fitting of a straight line with correlated errors," *Earth and planetary science letters*, vol. 5, pp. 320–324, 1968.
- [36] P. Viola and M. Jones, "Rapid object detection using a boosted cascade of simple features," in *Proceedings of the 2001 IEEE computer society conference on computer vision and pattern recognition. CVPR 2001*, vol. 1. IEEE, 2001, pp. 1–I.
- [37] R. Lienhart and J. Maydt, "An extended set of haar-like features for rapid object detection," in *Proceedings. international conference on image processing*, vol. 1. IEEE, 2002, pp. 1–I.
- [38] R. Lienhart, A. Kuranov, and V. Pisarevsky, "Empirical analysis of detection cascades of boosted classifiers for rapid object detection," in *Joint pattern recognition symposium*. Springer, 2003, pp. 297–304.
- [39] T. Huang, G. Yang, and G. Tang, "A fast two-dimensional median filtering algorithm," *IEEE Transactions on Acoustics, Speech, and Signal Processing*, vol. 27, no. 1, pp. 13–18, 1979.
- [40] K. Takita, T. Aoki, Y. Sasaki, T. Higuchi, and K. Kobayashi, "High-accuracy subpixel image registration based on phase-only correlation," *IEICE transactions on fundamentals of electronics, communications and computer sciences*, vol. 86, no. 8, pp. 1925–1934, 2003.
- [41] B. S. Reddy and B. N. Chatterji, "An fit-based technique for translation, rotation, and scale-invariant image registration," *IEEE transactions on image processing*, vol. 5, no. 8, pp. 1266–1271, 1996.
- [42] H. S. Stone, M. T. Orchard, E.-C. Chang, and S. A. Martucci, "A fast direct fourier-based algorithm for subpixel registration of images," *IEEE Transactions on geoscience and remote sensing*, vol. 39, no. 10, pp. 2235–2243, 2001.
- [43] H. Foroosh, J. B. Zerubia, and M. Berthod, "Extension of phase correlation to subpixel registration," *IEEE transactions on image processing*, vol. 11, no. 3, pp. 188–200, 2002.
- [44] T. Shimada, M. Ikebe, P. Ambalathankandy, M. Motomura, T. Asai *et al.*, "Sparse disparity estimation using global phase only correlation for stereo matching acceleration," in *2018 IEEE International Conference on Acoustics, Speech and Signal Processing (ICASSP)*. IEEE, 2018, pp. 1842–1846.
- [45] A. Telea, "An image inpainting technique based on the fast marching method," *Journal of graphics tools*, vol. 9, no. 1, pp. 23–34, 2004.

- [46] K. Tamura, T. Fujita, and Y. Morisaki, "Vacuum-sintered body of a novel apatite for artificial bone," *Open Engineering*, vol. 3, no. 4, pp. 700–706, 2013.
- [47] A. Pfeil, J. Böttcher, B. E. Seidl, J.-P. Heyne, A. Petrovitch, T. Eidner, H.-J. Mentzel, G. Wolf, G. Hein, and W. A. Kaiser, "Computer-aided joint space analysis of the metacarpal-phalangeal and proximal-interphalangeal finger joint: normative age-related and gender-specific data," *Skeletal radiology*, vol. 36, no. 9, pp. 853–864, 2007.
- [48] R. A. Brooks and G. Di Chiro, "Statistical limitations in x-ray reconstructive tomography," *Medical physics*, vol. 3, no. 4, pp. 237–240, 1976.
- [49] D. A. Chesler, S. J. Riederer, and N. J. Pelc, "Noise due to photon counting statistics in computed x-ray tomography," *Journal of computer assisted tomography*, vol. 1, no. 1, pp. 64–74, 1977.
- [50] C. Häger-Ross and M. H. Schieber, "Quantifying the independence of human finger movements: comparisons of digits, hands, and movement frequencies," *Journal of Neuroscience*, vol. 20, no. 22, pp. 8542–8550, 2000.